Characterization of Impurities in Nanomaterials

Kemi Y. Adewale and Mathew O. Aibinu

Abstract Nanomaterials have been known for varieties of applications. Interest in mixed metal-oxide nanoparticles stems mainly due to their unusual optical, electric, and magnetic properties. There are reports on the investigation of nanoferrous alloys for unique applications in medical imaging, hyperthermia, and drug targeting. In the last decade, considerable attention has been paid to overcome the miniaturization challenges facing the industries in the synthesis of magnetic and electronic devices such as ferrites. This study will set the phase for numerical characterization of the nonmagnetic ions whose dilution with nanoferrites improves the magnetic properties of the nanomaterials. The substitution of impurities into the different ferrite systems to improve their basic properties are presented. This research will help in the technological development that will further increase the understanding of researchers in physical and biological sciences.

Keywords Nanomaterials · Nanoparticles · Ferrite · Magnetic

K. Y. Adewale
School of Chemistry and Physics, University of KwaZulu-Natal, Westville Campus, Durban 4000, South Africa
e-mail: kemiadewale2@gmail.com; 217078608@stu.ukzn.ac.za

M. O. Aibinu (✉)
Institute for Systems Science & KZN E-Skill CoLab, Durban University of Technology, Durban 4000, South Africa
e-mail: moaibinu@yahoo.com; mathewa@dut.ac.za

DSI-NRF Centre of Excellence in Mathematical and Statistical Sciences (CoE-MaSS), Johannesburg, South Africa

National Institute for Theoretical and Computational Sciences (NITheCS), Stellenbosch, South Africa

K. Inal et al. (eds.), *NUMISHEET 2022*, The Minerals, Metals & Materials Series,
https://doi.org/10.1007/978-3-031-06212-4_3

Introduction

The technological importance of superparamagnetic ferrite materials has increased significantly over the last few decades [17, 29]. Progress in synthesis techniques has generated more interest in ferrites in order to improve their properties and expand their applications. Ferrites are ceramic magnetic materials with general chemical formula MFe_2O_4, where M represents one or a mixture of divalent transition metals such as Mn, Zn, Ni, Co, Cu, Fe, Mg, or Ca. Zinc ferrite ($ZnFe_2O_4$) possesses normal spinel structure and contains two different cationic sites; eight tetrahedral A-sites and sixteen octahedral B-sites. Zinc ions occupy exclusively the tetrahedral A sites while iron ions are only at the octahedral B sites. The distribution of cations determines the magnetic properties of spinel ferrites. Magnetic coupling in spinel ferrite occurs via super-exchange interactions. Super-exchange between two metal cations can occur via intermediate oxygen ions in the spinel structure through A-O-A, B-O-B, and A-O-B coupling. The magnetic behavior of ferrites is strongly influenced by the particle size, the preparation method, and structure [7]. Nanoparticles have sizes in the range from 1 to 100 nm and exhibit unique physical and chemical properties due to their high surface area and nanoscale size [21]. The size reduction of a magnetic material leads to novel properties like super-paramagnetism due to small volume compared to the corresponding bulk material. The optical properties of nanoparticles are reported to be dependent on the size, which imparts different colors due to absorption in the visible region. Other properties such as their reactivity and toughness also depend on their unique size, shape, and structure. These characteristics make the magnetic nanoparticles useful for various commercial and domestic applications, which include catalysis, magnetic resonance imaging, medical applications, energy-based research, and environmental applications.

Zinc substitution influences the magnetic properties of a nanoscale system [35]. There is a recent outline on the analysis of Mg-doped $ZnFe_2O_4$ [4]. Calcium and iron-based compounds have also been explored in the bulk form for optical memory devices, steel making industry (as deoxidizer, desulfuration, and dephosphorization) [19], as pigment [31], and as absorbent of hydrogen sulfide (H_2S) [18]. In comparison with other ferrites such as $MnFe_2O_4$, $NiFe_2O_4$, $CoFe_2O_4$ and $CuFe_2O_4$, $CaFe_2O_4$ has significant advantages. It is biocompatible and eco-friendly due to the presence of Ca^{2+} instead of the heavy metals. The synthesis and formation mechanism and magnetic properties in bulk form have also been considered [11, 20]. $CaFe_2O_4$ does not have the spinel structure due to the large size of the calcium ion which tends to be 8 or 9-fold coordinated [37]. Its structure is made of distorted FeO_6 octahedra calcium atoms and the phase transition is due to Fe^{3+} high spin/low spin transition [25]. There are few reports on the morphology, structure and magnetic properties of Ca-ferrites in the nano-regime (See e.g., [8]). A report on hematite-like structure of $CaFe_2O_4$ is given in [5].

Samples produced from different laboratories and by different techniques can show differences in their properties. The aim of this work is to determine the effects

of Ca^{2+} on the phase stability of $ZnFe_2O_4$, without any additional calcination and reduction steps. The reports on the synthesis, structural, magnetic, and morphological properties of Ca-doped $ZnFe_2O_4$ nanoparticles are given.

Experimental Details

Nanoferrites and nanocomposites of $Ca_xZn_{1-x}Fe_2O_4$ (x = 0, 0.02, 0.06, 0.08, 0.2, 0.5 0.6, 0.8, and 1) were prepared by the glycol-thermal method. The chemical reagents used were calcium chloride $CaCl_2.2H_2O$, zinc chloride $ZnCl_2$, and iron (III) chloride hexa-hydrate $FeCl_3.6H_2O$. All chemicals were of analytical grades. These were weighed in required proportions, then dissolved in about 50 ml of de-ionized water and magnetically stirred. Ammonia solution (NH_3) was slowly added to the mixture of chloride solutions under rapid stirring for about 10 min in order to initiate precipitation until a pH$\approx$ 10. The solution was further stirred for 40 min. The precipitate was mixed with 100 ml of ethylene glycol. The mixture was then placed in a 600 ml stainless steel pressure vessel (Watlow series model PARR 4843 reactor). The reactor was heated to a soak temperature of 200 °C and the gauge pressure was allowed to gradually rise to about 170 psi and angular speed of 300 rpm. These conditions were held for 6 h. The cooled reacted products were filtered and washed several times with de-ionized water and finally with ethanol over a Whatman filter in a Büchner flask in order to remove the chlorides. The absence of chlorides was confirmed by the addition of a standard solution of silver nitrate ($AgNO_3$) to the filtrate. The recovered synthesized samples were left to dry on the filter paper for 24 hrs under a 200 W infrared light. The dried products were then homogenized using an agate mortar and pestle. The samples were characterized at room temperature by X-ray diffraction (XRD) using a monochromatic beam of Co-K_α radiation (λ = 1.7903 Å), high-resolution transmission and scanning electron microscopy (HRTEM and HRSEM), ^{57}Fe Mössbauer spectroscopy and a vibrating sample magnetometer.

Results and Discussion

X-ray Diffraction

The XRD patterns of $Ca_xZn_{1-x}Fe_2O_4$ (x = 0, 0.02, 0.06, 0.08, 0.2, 0.5 0.6, 0.8, and 1) are given in Fig. 1. The calculated values of crystallite sizes D, lattice parameter a, and the X-ray density ρ are presented in Table 1. The peaks were correctly indexed and matched with documented XRD patterns and no impurity phase was detected in all the samples [22, 23]. The peaks in x=0, 0.02 and 0.06 correspond to a single phase cubic spinel structure. A mixed phase of a spinel and a hematite-like structure started to evolve at x = 0.08. A nanocomposite of a spinel and a hematite-like structure is

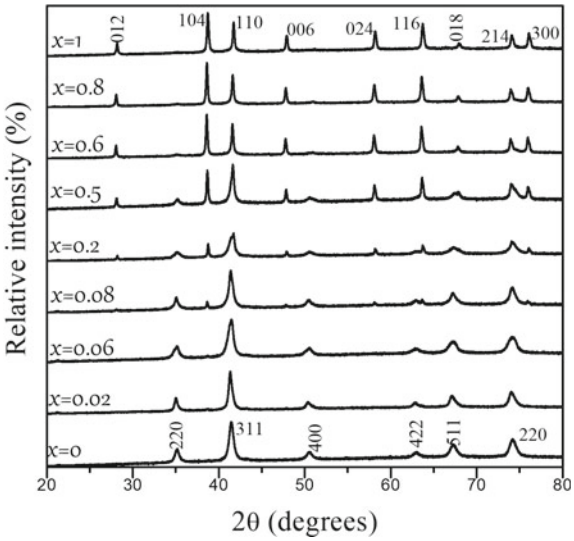

Fig. 1 XRD patterns of $Ca_xZn_{1-x}Fe_2O_4$, **a** $x = 0,\ 0.02, 0.06, 0.08, 0.2, 0.5, 0.6, 0.8$ and 1

Table 1 Crystallite size (D), lattice parameters (a) and X-ray densities ρ_{XRD} for prepared samples of $Ca_xZn_{1-x}Fe_2O_4$ ($x = 0,\ 0.02,\ 0.06,\ 0.08,\ 0.2,\ 0.5,\ 0.6,\ 0.8$, and 1)

Sample x	Composition	Spinel			Hematite		
		D (nm) ±0.4	a (Å) ±0.006	ρ_{XRD} (g/cm^3) ±0.28	D (nm) ±0.94	a (Å) ±0.01	ρ_{XRD} (g/cm^3) ±0.48
0	$ZnFe_2O_4$	18.6	8.386	5.43	–	–	–
0.02	$Ca_{0.02}Zn_{0.98}Fe_2O_4$	23.1	8.407	5.38	–	–	–
0.06	$Ca_{0.06}Zn_{0.94}Fe_2O_4$	16.0	8.399	5.37	–	–	–
0.08	$Ca_{0.08}Zn_{0.92}Fe_2O_4$	23.4	8.401	5.36	63.40	11.15	2.29
0.2	$Ca_{0.2}Zn_{0.8}Fe_2O_4$	17.0	8.375	5.34	63.44	11.12	2.28
0.5	$Ca_{0.5}Zn_{0.5}Fe_2O_4$	24.2	8.376	5.16	54.62	11.14	2.19
0.6	$Ca_{0.6}Zn_{0.4}Fe_2O_4$	–	–	–	52.48	11.17	2.15
0.8	$Ca_{0.8}Zn_{0.2}Fe_2O_4$	–	–	–	54.41	11.16	2.11
1	$CaFe_2O_4$	–	–	–	45.42	11.13	2.08

formed at $x = 0.2$ and 0.5. Complete hematite-like structures were observed at $x = 0.6$, $x = 0.8$ and 1. The increase in the addition of Ca^{2+} ion concentration makes the diffraction peaks sharper and narrower [9]. This is a one-step technique for the synthesis of $CaFe_2O_4$ and it gives clear and sharp diffraction peaks. This is an interesting result compared to other reports where $CaFe_2O_4$ was synthesized by more than one-step or at a much-elevated temperature [13, 33]. Using the Debye-Scherrer formula,

$$D = \frac{K\lambda}{W_{hkl}\cos\theta}, \tag{1}$$

where K is a constant associated with the shape factor usually taken to be 0.9 for particles of unknown shape, 0.89 for particles with spherical shape and 0.94 for cubic particles. The wavelength for the monochromatic X-ray beam is $\lambda = 1.7903$ Å and W_{hkl} is the full width at half maximum (FWHM) of the broadening line diffraction peak of the most prominent peak and θ is the Bragg angle. The crystallite sizes (D) for the pure cubic spinel phases were calculated from the most intense 311 peak, while for the mixed phase, 220 peak was used for the spinel and 104 peak for the hematite phases. The lattice parameters were obtained using

$$a = \frac{\lambda}{2\sin\theta}\sqrt{h^2 + k^2 + l^2}, \tag{2}$$

where h, k and l are known as the Miller indices for the diffracting planes and the X-ray density using

$$\rho_{XRD} = \frac{8M}{N_A a^3}, \tag{3}$$

where 8 is the number of molecules per unit, M is the molecular weight, N_A is the Avogadro's constant and a is the size of the lattice parameter that defines the size of the unit cell [3]..

The strong and sharp diffraction peaks indicate good crystallinity of the samples [9]. This suggests an increase in particle size. The present results indicate that at $x = 0$, 0.02, 0.06, 0.08, 0.2, and 0.5, the lattice parameter a and crystallite size D of the cubic spinel structures varies. The lattice parameters a and crystallite size D of the hematite phase increased for $x = 0.08$, 0.2, and 0.5. However, at $x = 0.6$, 0.8, and 1, the lattice parameter a decreased while the crystallite size D varies for the hematite phase as the Ca^{2+} ion concentration increases. The variation of the size of the obtained particles is between 19 nm and 63 nm.

Morphology Study

The morphology and micro-structure of the nanoparticles were investigated by HRSEM and HRTEM measurements. Figures 2 and 3 show the HRSEM and HRTEM micrographs of the samples. The particles are almost spherical in shape as seen in

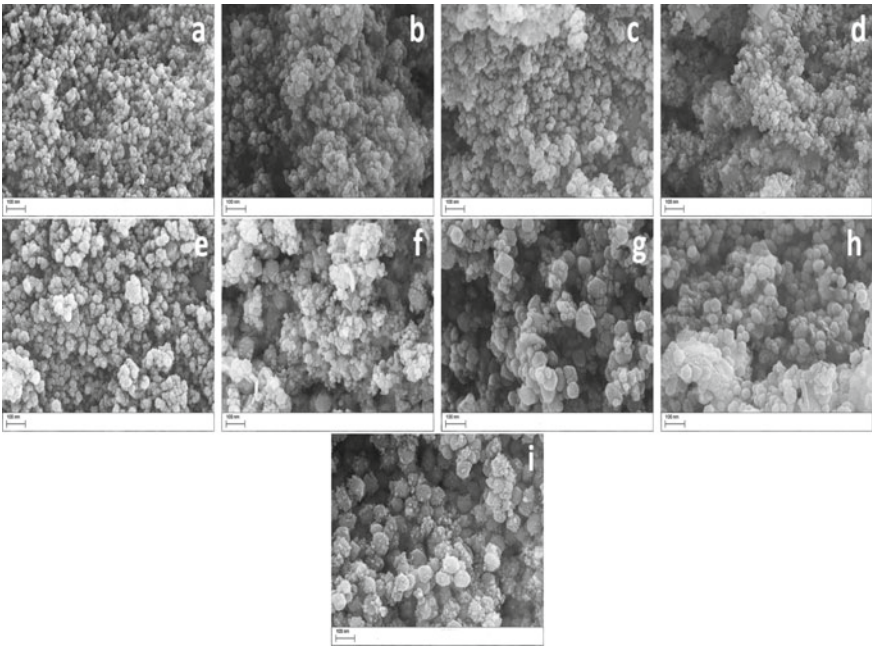

Fig. 2 HRSEM images of $Ca_xZn_{1-x}Fe_2O_4$, **a** $x = 0$, **b** $x = 0.02$, **c** $x = 0.06$, **d** $x = 0.08$, **e** $x = 0.2$, **f** $x = 0.5$, **g** $x = 0.6$, **h** $x = 0.8$, and **i** $x = 1$

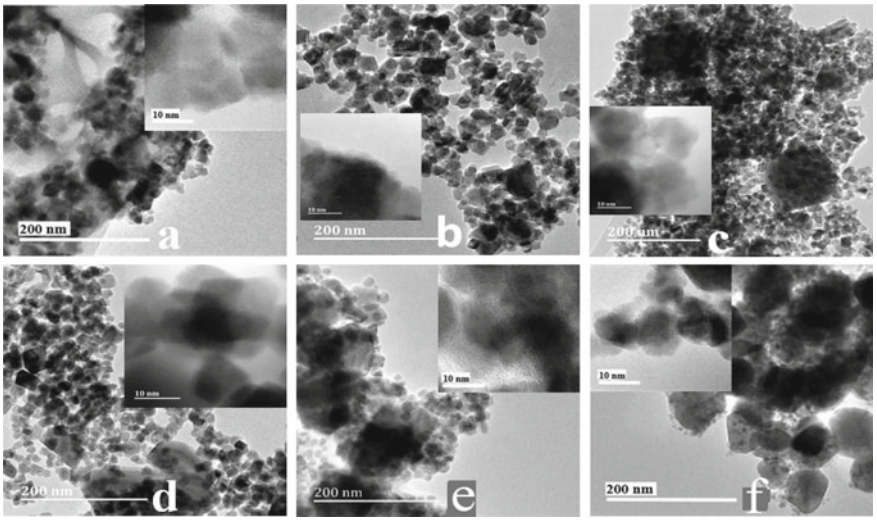

Fig. 3 Selected HRTEM images of $Ca_xZn_{1-x}Fe_2O_4$, **a** $x = 0$, **b** $x = 0.02$, **c** $x = 0.06$, **d** $x = 0.2$, **e** $x = 0.5$, and **f** $x = 1$

the images. The particle size increased significantly as the Ca^{2+} ion concentration increases. This is due to the replacement of Zn^{2+} which has a smaller ionic radius of 0.74 Å, [1], with Ca^{2+} which has larger ionic radius of 0.99 Å, [27]. This is in good agreement with the results obtained from the XRD measurements. The pure samples are $ZnFe_2O_4$ and $CaFe_2O_4$ in Fig. 2 of HRSEM. In the figure, the 3d and 3e show a mixed phase of cubic spinel and a hematite-like structure for $Ca_{0.2}Zn_{0.8}Fe_2O_4$ and $Ca_{0.5}Zn_{0.5}Fe_2O_4$. These show a clear distinction of the nanocomposite for mixed phases as compared to pure cubic spinel structure of doped samples $Ca_{0.02}Zn_{0.8}Fe_2O_4$ and $Ca_{0.06}Zn_{0.5}Fe_2O_4$ [10].

Mössbauer Measurements

The room temperature ^{57}Fe Mössbauer spectroscopy is presented in Fig. 4. The calibration was done using α-Fe foil at a constant acceleration. The magnetic components of the spectra were fitted using the Lorentzian site analysis. The spectrum for $x = 0$ was best fitted with two sextets and two doublets. Two sextets and one doublet were used to fit $x = 0.02$, 0.06, 0.6, and 0.8. The spectra for $x = 0.2$, 0.5, and 1 exhibit three sextets and one doublet. The two sextets for the samples $x = 0$, 0.02, and 0.06 are associated with the coordination of Fe^{3+} ions at tetrahedral *A* and octahedral *B* sites of the spinel crystal structure [16]. The sextets having large hyperfine magnetic field are assigned to the hematite-like structure of the materials [24]. The other two sextets are attributed to Fe^{3+} at tetrahedral *A* and octahedral *B* sites, based on the nature of their hyperfine magnetic field values (hyperfine magnetic field at *B* sites

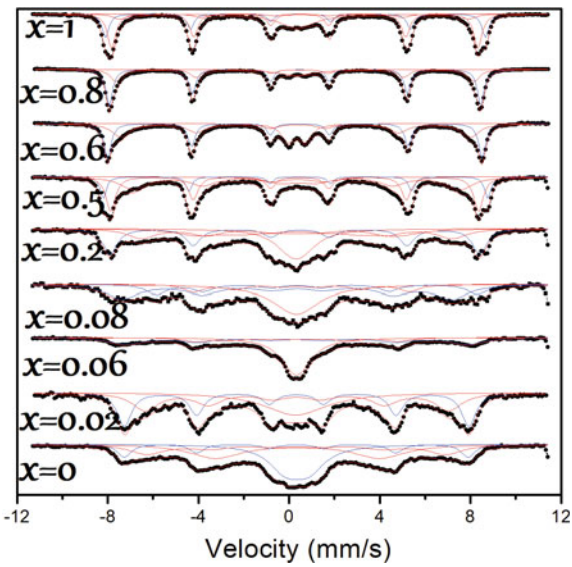

Fig. 4 Fitted room temperature ^{57}Fe Mössbauer spectra of $Ca_xZn_{1-x}Fe_2O_4$ ($x = 0$, 0.02, 0.06, 0.08, 0.2, 0.5, 0.6, 0.8, and 1) nanoferrites

is greater than the hyperfine field at *A* sites) [28]. The doublets are associated with small nanoparticles in paramagnetic states. It was observed that the obtained isomer shift values are less than 0.6 mm/s. This leads to the deduction that only Fe^{3+} is present and ruling out the detectable presence of Fe^{2+} ions [34]. The higher values of quadrupole splitting indicate that the ions are embedded in noncubic surroundings [12, 14], while the relatively small values of the quadrupole splitting indicate that *A* and *B* sites have nearly cubic symmetry [12]. The larger line width on the A- and B-sites are attributed to the magnetic dipolar effects [26, 36]. The hyperfine magnetic field reported here are in the range of the reported values for α-Fe_2O_3 [5, 23].

Magnetization Measurements

The hysteresis loops measured at room temperature performed in a magnetic field of up to 14 kOe are shown in Fig. 5. The values of coercive fields (H_C), saturation magnetizations (M_S), residual magnetizations (M_R), and squareness of the loops (M_R/M_S) are calculated from the hysteresis loops and the results are presented in Table 2. Figures 6, 7 and 8, respectively, display the variation of H_C, M_S, and M_R with respect to x. We obtained the coercive field from

$$H_C = \left| \frac{H_{C1} + H_{C2}}{2} \right| \tag{4}$$

For the pure spinel and mixed phase samples, it was observed that there is variation in the coercive fields as x increases. However, as for the pure hematite structure samples, there is decrease in values of the coercive fields as x increases. This observation compares well with the Mössbauer results which can be attributed to fewer magnetic

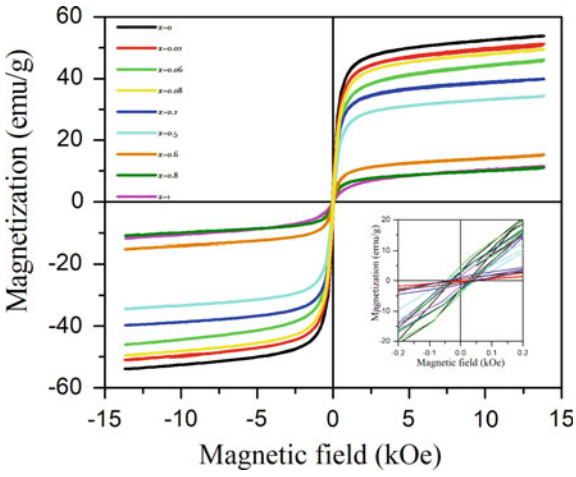

Fig. 5 Room temperature hysteresis loops of $Ca_xZn_{1-x}Fe_2O_4$ (x = 0, 0.02, 0.06, 0.08, 0.2, 0.5, 0.6, 0.8, and 1) nanoferrites

Table 2 Coercivity H_C, saturation magnetization M_S, remanence magnetization M_R and squareness ratio (M_R/M_S) obtained at room temperatures in applied field of 14 kOe for $Ca_xZn_{1-x}Fe_2O_4$ ($x = 0,\ 0.02,\ 0.06,\ 0.08,\ 0.2,\ 0.5,\ 0.6,\ 0.8$, and 1)

x	H_C (Oe) ± 1	M_S (emu/g) ±0.5	M_R (emu/g) ±0.5	M_R/M_S ±0.03	K (emu kOe/g) ±0.03	p (psi)
0	25	49.1	2.9	0.05	1.28	170
0.02	44	46.87	4.5	0.09	2.15	170
0.06	36	41.52	3.1	0.08	1.56	170
0.08	30	45.93	0.6	0.01	1.44	180
0.2	21	38.3	1.7	0.04	0.84	180
0.5	51	31.15	3.2	0.10	1.66	170
0.6	49	8.28	1.2	0.14	0.42	170
0.8	36	6.61	0.6	0.09	0.25	180
1	15	7.92	0.1	0.01	0.12	180

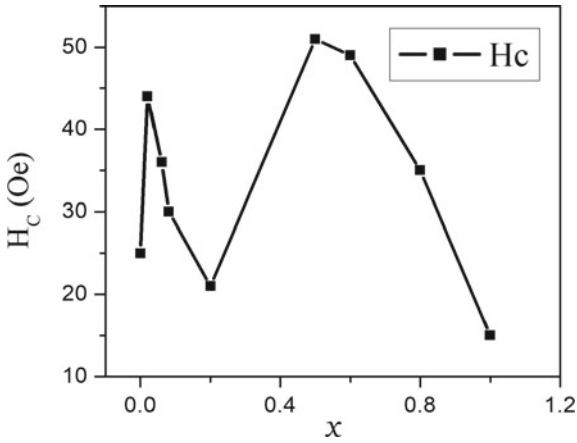

Fig. 6 Variation of coercive field H_C with x.

neighbours as a result of substitution of Zn^{2+} by Ca^{2+} ions. The M_S were estimated using the equation for the law of approach to saturation magnetization

$$M(H) = M_S\left(1 - \frac{a}{H} - \frac{b}{H}^2\right) + \chi H, \tag{5}$$

where M_S, a, b and χ are the best fit parameters to the data. The low squareness (M_R/M_S ratios) and the small H_C values reflected the superparamagnetic behavior of the samples [2, 38]. The obtained magnetic squareness values for $x = 0,\ 0.02,\ 0.06,\ 0.08\ 0.2, 0.5, 0.6\ 0.8$ and 1, are 0.05, 0.09, 0.08, 0.01, 0.04, 0.10, 0.14, 0.09. 0.10, and 0.01, respectively. Since the values are in the range of 0.1 for superparamagnetic materials [15], this supports the superparamagnetic nature of the samples. It was

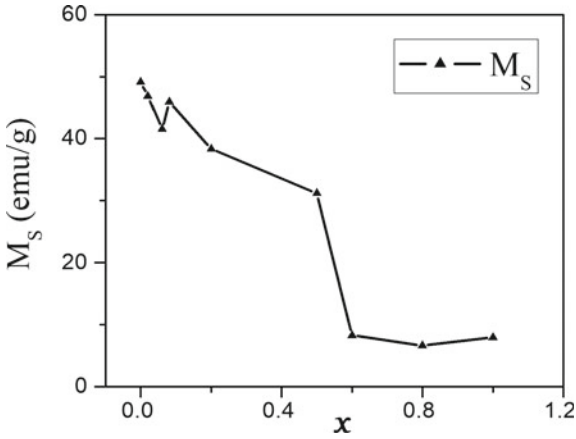

Fig. 7 Variation of saturation magnetization M_S with x.

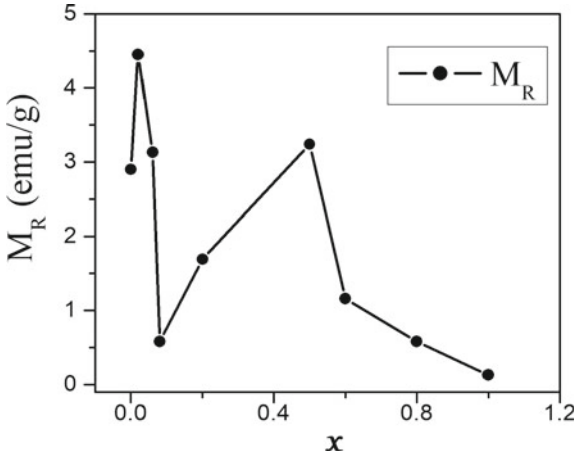

Fig. 8 Variation of remanent magnetization M_R with x.

observed that the saturation magnetization decreases as the Ca^{2+} ion concentration increases. This observation agrees with the reports in the literature [32]. The decrease in M_S can be attributed to the formation of hematite-like phase [6].

Conclusion

$Ca_xZn_{1-x}Fe_2O_4$ nanoferrites were synthesized via glycol-thermal method. The prepared samples were characterized by XRD, HRTEM, HRSEM, Mössbauer spectroscopy, and magnetization measurements. XRD results show single phase cubic spinel structure for x = 0, 0.02, and 0.06. For x = 0.08, 0.2, and 0.5, the XRD results show mixed phases of cubic spinel and hematite-like structures, while for

x=0.6, 0.8, and 1, the observed phase is a pure hematite-like structure. Crystallite sizes were obtained in the range 19–63 nm, which appear to be influenced by the increasing value of x. The substitution of Zn^{2+} for larger amounts of Ca^{2+} increased the crystallite size of the sample. A gradual increase in the lattice parameter was also observed with increasing Ca content. Results also show a strong correlation between the XRD density with Ca concentration x, that is, as x increases the XRD density decreases. The HRTEM and HRSEM images show clearly nanocrystalline nature of the samples. HRTEM reveals the clear differences in the morphologies of the samples. ^{57}Fe Mössbauer spectroscopy results which were measured at room temperature show transformation to higher magnetic hyperfine fields for the samples with pure hematite-like structural phase. The magnetization measurements at room temperature show evidence of superparamagnetic behaviour of the compounds. It is interesting to note that there is variation in the saturation magnetization of the samples with mixed phase, while the saturation magnetization for the pure hematite phase reduced drastically with increasing amount of x. The decrease in magnetization is attributed to the formation of the hematite-like phase or cation distribution in A- and B-sites.

Acknowledgements The second author acknowledges with thanks the postdoctoral fellowship and financial support from the DSI-NRF Center of Excellence in Mathematical and Statistical Sciences (CoE-MaSS). Opinions and conclusions are those of the authors and are not necessarily to be attributed to the CoE-MaSS.

References

1. Abdallah HMI, Moyo T (2013) Structural and magnetic studies of $(Mg, Sr)_{0.2}Mn_{0.1}Co_{0.7}Fe_2O_4$ nanoferrites. J Alloys Comput 562:156–163. https://doi.org/10.1016/j.jallcom.2013.02.056
2. Abdallah HMI, Moyo T (2012) The influence of annealing temperature on the magnetic properties of $Mn_{0.5}Co_{0.5}Fe_2O_4$ nanoferrites synthesized via mechanical milling method. J Supercond Nov Magn 26:1361–1367
3. Abdallah HMI, Moyo T, Msomi JZ (2011) Mössbauer and electrical studies of $Mn_xCo_{1-x}Fe_2O_4$ compounds prepared via glycothermal route. J Supercond Nov Magn 24:669
4. Adewale KY, Ezekiel IP, (2020) Synthesis and characterization of Mg doped $ZnFe_2O_4$. reseach and reviews. J Phys 9(1):57–65
5. Adewale ky, Ezekiel IP, (2019) Magnetic and Mössbauer studies of $Ca_xZn_{1-x}Fe_2O_4$ nanoferrites. Int J Solid State Mater 5(2):23–28
6. Airimioaei M, Ciomaga CE, Apostolescu N, Leontie L, Iordon AR, Mitoseriu L, Palamaru MN (2011) Synthesis and functional properties of the $Ni_{1-x}Mn_xFe_2O_4$ ferrites. J Alloy Compd 509:8065–8072. https://doi.org/10.1016/j.jallcom.2011.05.034
7. Aisida SO, Akpa PA, Ishaq Ahmad M, Maaza Ezema FI (2019) Influence of PVA, PVP and PEG doping on the optical, structural, morphological and magnetic properties of zinc ferrite nanoparticles produced by thermal method. Physica B: Condensed Matter 571:130–136. https://doi.org/10.1016/j.physb.2019.07.001
8. Almessiere MA, Slimani Y, Auwal IA, Shirsath SE, Gondal MA, Sertkol M, Baykal A (2021) Biosynthesis effect of Moringa oleifera leaf extract on structural and magnetic properties of Zn doped Ca-Mg nano-spinel ferrites. Arab J Chem 14(8):103261. https://doi.org/10.1016/j.arabjc.2021.103261

9. Barsoum MW (2019) Fundamentals of ceramics, 2nd edn. CRC Press. https://doi.org/10.1201/9781498708166
10. Bertaut F, Blum P, Magnano G (1955) Structure of the monocalcium vanadite, chromite and ferrite. Compt Rend Acad Sci Paris 241:757–759
11. Candeia RA, Bernardi MIB, Longo E, Santos IMG, Souza AG (2004) Synthesis and characterization of spinel pigment $CaFe_2O_4$ obtained by the polymeric precursor method. Mater Lett 58:569–572
12. Birchall T, Greenwood NN, Reid AF (1969) Mössbauer, electron resonance, optical, and magnetic studies of iron(III) in oxide host lattices. J Chem Soc A 2382–2398
13. Das AK, Govindaraj R, Srinivasan A (2018) Structural and magnetic properties of sol-gel derived $CaFe_2O_4$ nanoparticles. J Magn Magn Mater 451:526–531, 103261. https://doi.org/10.1016/j.jmmm.2017.11.102
14. DeBenedetti S, Lang G, Ingalls R (1961) Electric quadrupole splitting and the nuclear volume effect in the ions of Fe^{57}. Phys Rev Lett 6:60. https://doi.org/10.1103/PhysRevLett.6.60
15. Debnath A, Bera A, Chattopadhyay KK, Saha B (2016) Studies on magnetic properties of chemically synthesized crystalline calcium ferrite nanoparticles. AIP Conf Proc 1731:050103. https://doi.org/10.1063/1.4947757
16. Gismelseed AM, Mohammed HM, Widatallah HM, Al-Rawas AD, Elzain ME, Yousif A (2010) Structure and magnetic properties of the $Zn_xMg_{1-x}Fe_2O_4$ ferrites. J Phys: Conf Ser 217:012138
17. Hirabayashi D, Sakai Y, Yoshikawa T, Mochizuki K, Kojima Y, Suzuki K, Ohshita K, Watanabe Y (2006) Mössbauer characterization of calcium-ferrite oxides prepared by calcining Fe_2O_3 and CaO. Hyperfine Interact 167:809–813
18. Jain TK, Morales MA, Sahoo SK, Leslie-Pelecky DL, Labhasetwar V (2005) Ironoxide nanoparticles for sustained delivery of anticancer agents. Mol Pharm 2:194–205
19. Jalil RA, Zhang Y (2008) Biocompatibility of silica coated NaYF(4) upconversion fluorescent nanocrystals. Biomaterials 29:4122–4128
20. Jeon JW, Jung SM, Sasaki Y (2010) Formation of calcium ferrites under controlled oxygen potentials at 1273 K. ISIJ Int 50(8):1064–1070
21. Khan I, Saeed K, Khan I (2019) Nanoparticles: Properties, applications and toxicities. Arab J Chem 12(7):908–931. https://doi.org/10.1016/j.arabjc.2017.05.011
22. Khanna L, Verma NK (2013) Size-dependent magnetic properties of calcium ferrite nanoparticles. J Magn Magn Mater 336:1–7, 012138
23. Hirabayashi D, Sakai Y, Yoshikawa T, Mochizuki K, Kojima Y, Suzuki K, Ohshita K, Watanabe Y (2006) Mössbauer characterization of calcium-ferrite oxides prepared by calcining Fe_2O_3 and CaO. Hyperfine Interact 167:809. https://doi.org/10.1007/s10751-006-9362-x
24. Lavela P, Tirado JL (2007) $CoFe_2O_4$ and $NiFe_2O_4$ synthesized by sol-gel procedures for their use as anode materials for Li ion batteries. J Power Sour 172:379–387. https://doi.org/10.1016/j.jpowsour.2007.07.055
25. Li X, Chen C, Zhang F, Fang H, Huang X, Yi Z (2021) Photostriction of ferrites under visible light. ACS Appl Electron Mater 3(6):2534–2542, 012138. https://doi.org/10.1021/acsaelm.1c00077
26. Lu SP, Evan BJ (1976) High temperature electronic structure of Fe_3O_4. AIP Conf Proc 34:181. https://doi.org/10.1063/1.2946059
27. McBride MB, Frenchmeyer M, Kelch SE, Aristilde L (2017) Solubility, structure, and morphology in the co-precipitation of cadmium and zinc with calcium-oxalate. J Colloid Interface Sci 486:309–315. https://doi.org/10.1016/j.jcis.2016.09.079
28. Meena SS, Srinivas Ch, Sudarsan V, Tirupanyam BV, Rao KR, Sastry DL, Yusuf SM (2012) Mössbauer spectroscopic study of heat-treated $(Ni_{0.5}Zn_{0.5})Fe_2O_4$ nanoparticles. AIP Conf Proc 1447:231–1245, 012138. https://doi.org/10.1063/1.4710463
29. Pandey B, Litterst FJ, Baggio-Saitovitch EM (2015) Preferential spin canting in nanosize zinc ferrite. J Magn Magn Mate 385:412–417
30. Pettit GA, Forester DW (1971) Mössbauer study of cobalt-zinc ferrites. Phys Rev B 4:3912

31. Ruan J, Wang K, Song H, Xu X, Ji JJ, Cui DX (2011) Biocompatibility of hydrophilic silica-coated CdTe quantum dots and magnetic nanoparticles. Nanoscale Res Lett 6(299):1–13
32. Shobana MK, Sankar S (2009) Structural, thermal and magnetic properties of $Ni_{1-x}Mn_xFe_2O_4$ nanoferrites. J Magn Magn Mater 321:2125–2128
33. Sulaiman NH, Ghazali MJ, Majlisb BY, Yunas J, Razali M (2015) Superparamagnetic calcium ferrite nanoparticles synthesized using a simple sol-gel method for targeted drug delivery. Bio-Med Mater Eng 26:S103–S110. https://doi.org/10.3233/BME-151295
34. Sorescu M, Diamandesu L, Peelamedu R, Roy R, Yadiji P (2004) Structural and magnetic properties of NiZn ferrites prepared by microwave sintering. J Magn Magn Mater 279:195–201. https://doi.org/10.1016/j.jmmm.2004.01.079
35. Tiwari P, Verma R, Kane SN, Tatarchuk T, Mazaleyrat F (2019) Effect of Zn addition on structural, magnetic properties and anti-structural modeling of magnesium-nickel nano ferrites. Mater Chem Phys 229:78–86. https://doi.org/10.1016/j.matchemphys.2019.02.030
36. Van D (1977) Magnetic and structural phase transitions in sodium intercalates Na_xVS_2 and Na_xVSe_2. Physica 955:86-88B. https://doi.org/10.1016/0378-4363(77)90782-3
37. Vigneswari T, Raji P (2017) Structural and magnetic properties of calcium doped nickel ferrite nanoparticles by co-precipitation method. J Mol Struct 1127:515–521. https://doi.org/10.1016/j.molstruc.2016.07.116
38. Zheng W, Gao F, Gu H (2005) Magnetic polymer nanospheres with high and uniform magnetite content. J Magn Magn Mater 288:403–410, 012138